journal of the mechanical behavior of biomedical materials 128 (2022) 105098

Contents lists available at ScienceDirect

Journal of the Mechanical Behavior of Biomedical Materials

journal homepage: www.elsevier.com/locate/jmbbm

Shape optimization of orthopedic porous scaffolds to enhance mechanical performance

Ali H. Foroughi , Mir Jalil Razavi *

Department of Mechanical Engineering, Binghamton University, State University of New York, New York, 13902, USA

ARTICLE INFO

Keywords:
Bone scaffolds
MFCC scaffolds
Stiffness
Topology optimization
Finite element method

ABSTRACT

Polymeric bone scaffolds are supposed to temporarily bear the external mechanical forces applied to the injured area. The implanted scaffolds should satisfy both mechanical and cell-proliferation requirements. In this study, to design an optimum scaffold structure from mechanical and cell growth perspectives, a new scaffold structure named MFCC (Modified Face Centered Cubic) is introduced, which is based on the Face Centered Cubic (FCC) arrangement of spherical pores. The geometric parameters of the scaffold structure are optimized to increase the stiffness of the scaffolds with 70%, 75%, and 80% porosities. The optimized MFCC scaffolds satisfy the cell growth requirements and show greater elastic modulus compared to regular OCS (Orthogonal Cylindrical Struts) scaffolds. For validation, the designed scaffolds made by the finite element optimization process were 3D printed, tested and compared with the OCS scaffolds. The results show that the gradual cross-section variation of the spheres in the optimized scaffold reduces the stress concentration and distributes the applied mechanical loads more uniformly compared to OCS scaffolds. Moreover, from the cell growth perspective, a spherical pore with a concave surface provides a better surface for the proliferation of cells. The optimized MFCC scaffolds are stiffer in small strains and have a greater apparent yield stress compared to the OCS scaffolds at the same porosity. The enhancement in the stiffness of the scaffold is shape attributed and is independent of the material used. Therefore, the same percentage increase in the stiffness is achievable for a broad range of materials. The presented new design with improved stiffness helps to enhance the quality of load-bearing scaffolds.

1. Introduction

Porous scaffolds are used as bone grafts to provide a temporary support in the injured regions (Amini et al., 2012). From a cell proliferation point of view, a good bone scaffold is expected to have interconnected pores with optimum size and porosity to provide an appropriate medium for bone ingrowth (Grémare et al., 2018). An optimum porous architecture also needs to deliver adequate mechanical properties consistent with the implantation site (Chen et al., 2019).

Two distinct approaches are taken to enhance the mechanical response of a porous scaffold: the material modification and the geometry optimization. Scaffolds made of various composite and non-composite materials have been studied from the mechanical performance point of view (Liao et al., 2004; Naderi et al., 2021; Yin et al., 2019). In addition to the scaffold material, the geometry of the scaffold structure plays an essential role in improving the mechanical performance of the scaffold. Depending on the injured bone tissue and its loading conditions, different mechanical performance criteria are studied which include elastic response (Entezari et al., 2016; Skalka et al., 2019; Wieding et al., 2014), fatigue behavior (Kelly et al., 2019; Senatov et al., 2016), creep and impact strength (Niaza et al., 2017; Senatov et al., 2016). Because bone growth is regulated by the mechanical environment (Liedert et al., 2005), the stiffness of scaffold plays an essential role in the enhancement of bone formation. Therefore, the effective elastic modulus is an essential factor in bone scaffold investigations.

A bone scaffold is expected to have a comparable stiffness with the bone of the implantation site. Metallic alloys typically have a higher Young's modulus (100–220 GPa (Findik, 2017; Navarro et al., 2008)) than that of human bone (4–30 GPa (Alomari et al., 2018; Zhao et al., 2018)). This stiffness mismatch between the implant and the host bone may result in stress shielding, osteopenia, and bone fracture (Limmahakhun et al., 2017; Liverani et al., 2021). Therefore, biocompatible and bioresorbable polymeric materials such as PLA are being considered as scaffold material (Gregor et al., 2017; Rodrigues et al., 2016; Zhang et al., 2021). The lower Young's modulus of polymeric materials compared with human bone requires designers to enhance the scaffold

* Corresponding author.
E-mail address: mrazavi@binghamton.edu (M.J. Razavi).

https://doi.org/10.1016/j.jmbbm.2022.105098
Received 23 September 2021; Received in revised form 2 November 2021; Accepted 17 January 2022
Available online 29 January 2022

Nomenclature

CAD	Computer Aided Design
FCC	Face Centered Cubic
FDM	Fused Deposition Modeling
FEM	Finite Element Modeling
FE	Finite Element
MFCC	Modified Face Centered Cubic
NaN	Not a Number
OCS	Orthogonal Cylindrical Struts
PLA	poly(lactic acid)
TPMS	Triply Periodic Minimal Surface
a	Size of the MFCC scaffold unit cell
A_c	Full cross section area of scaffold normal to the compression direction
A_{mean}	Average surface area of scaffold normal to the compression direction
C	Geometry constant
C_1 to C_6	Optimization Constraints
D	Diameter of strut in OCS scaffolds
E_{bulk}	Young's modulus of bulk specimen
E_{eff}	Effective Young's modulus of scaffold
$\bar{E}_{eff}$	Normalized effective Young's modulus of scaffold
$E(m)$	Complete elliptic integral of the second kind
E_{MFCC}	Stiffness of MFCC scaffold
E_{OCS}	Stiffness of OCS scaffold
h	Diameter of the intersection throats (MFCC scaffold)
$K(m)$	Complete elliptic integral of the first kind
L_0	Initial length of scaffold in the compression direction
LA	Layer adhesion (OCS scaffold)
m	A parameter in complete elliptic integral
$P_{\max}$	Maximum pore size based on bone cell growth requirements
$P_{\min}$	Minimum pore size based on bone cell growth requirements
P_x	Pore size in direction x (OCS scaffold)
r	A parameter defined to calculate interconnection throat size
r_c	Radius of corner spherical pores
$\bar{r}_c$	Normalized radius of corner spherical pores
r_{cj}	Radius of corner spherical pores in the jth loop of the optimization
r_{cmax}	Upper bound of the radius of corner spherical pores (MFCC scaffold)
r_{cmin}	Lower bound of the radius of corner spherical pores (MFCC scaffold)
r_f	Radius of face spherical pores
$\bar{r}_f$	Normalized radius of face spherical pores
r_{fi}	Radius of face spherical pores in the ith loop of the optimization
r_{fmax}	Upper bound of the radius of face spherical pores (MFCC scaffold)
r_{fmin}	Lower bound of the radius of face spherical pores (MFCC scaffold)
R	A parameter defined to calculate the interconnection throat size
R_1 to R_5	Regions on the scaffold
RF	Reaction force
S_c	Corner spherical pore of MFCC scaffold
S_f	Face spherical pore of MFCC scaffold
$S_{\max}$	Maximum von Mises stress
S_v	Specific surface area
t_0	An angle in the elliptic integral formula
V_c	Volume of corner spherical pore (MFCC scaffold)
V_{cube}	Volume of cube
V_f	Volume of face spherical pore (MFCC scaffold)
V_{int}	Volume of intersection
V_{pore}	Volume of pore
V_s	Volume of cylindrical struts of the scaffold
w_a to w_f	Width of vertical pillars of MFCC scaffold
Y	Apparent yield point of scaffold
φ	Porosity of scaffold
φ_0	A specific porosity of scaffold
φ_{0k}	A specific porosity of scaffold in the kth loop of the optimization
ε_0	Compressive strain
$\Delta E\%$	Percentage change of the stiffness
ΔL	Length change of scaffold in the compression direction

stiffness by modifying the material properties (Li et al., 2021; Wang et al., 2021) and optimizing the pore architecture (Hu et al., 2019; Sahmani et al., 2020). One step towards this goal is optimization of the internal architecture of polymeric scaffolds to guarantee that the stiffness is maximum from a topological perspective.

In addition to the mechanical performance of the scaffold, the tissue regeneration rate is also influenced by the topology of the porous scaffolds. The effect of topological parameters such as curvature, pore geometry, and porosity on cell growth has been widely studied (A. Zadpoor, 2015; Bidan et al., 2013; Knychala et al., 2013; Rumpler et al., 2008). The cell proliferation rate increases with the curvature, and is larger on concave surfaces compared to planar and convex surfaces (Bidan et al., 2013; Knychala et al., 2013; Rumpler et al., 2008). The size of osteoblasts is in the range of 10–15 μm, which is a lower bound for the pore size of scaffolds (Qiu et al., 2019). The newly formed blood vessels also require some space to deliver nutrients and oxygen to the osteoblastic activity. Therefore, *in vivo* studies show that pores much larger than the size of bone cells are needed for optimal cell proliferation (Roosa et al., 2010). However, the reported values in the literature for the optimum porosity and pore size for bone cell growth are inconsistent (Chen et al., 2020; Diao et al., 2018; Lee et al., 2019; Murphy et al., 2010; Ouyang et al., 2019; Torres-Sanchez et al., 2017; Zaharin et al., 2018). As a rough estimate, a pore size in the range of 400–800 μm, and a minimum porosity of 50% are optimal values to avoid pore blockage and to provide adequate space for vascularization, cell adhesion, and cell proliferation (Abbasi et al., 2020; Buj-Corral et al., 2018).

The mechanical and biological requirements impose multiple constraints on the geometry of the scaffold. There are two approaches to create interconnected porous structures: construction of stochastic foams (Gualandi et al., 2010; Jing et al., 2019) and generation of the scaffolds based on unit-cell structures (Yang et al., 2020; Zaharin et al., 2018). Several efforts have been made to control the architecture of stochastic foam scaffolds (Behl et al., 2020; Novotna et al., 2019). However, it is much easier to adjust the architecture of a porous scaffold constructed by the unit-cell based approach. A straightforward modification of the pore shape and porosity of the scaffold structure enables designers to enhance the mechanical properties such as the elastic modulus and mechanical strength (Ambu and Morabito, 2018; Hedayati et al., 2016; Kadkhodapour et al., 2015; Soro et al., 2019; Zaharin et al., 2018). Additionally, by utilizing the unit-cell based design, porous architecture can be modified effortlessly to satisfy the cell-growth requirements (Chen et al., 2020; Onal et al., 2018; Sanz-Herrera et al., 2008; Van Bael et al., 2012). Different cellular lattice structures have been proposed in the literature to construct porous scaffolds, which range from simple ones that have orthogonal cylindrical struts (referred to as OCS scaffolds in this study) (Baptista et al., 2020; Gregor et al., 2017) to more complex ones that are inspired mostly by natural structures (Castro et al., 2019; Liu et al., 2018). The effect of topological

parameters such as porosity, surface area, laydown pattern, and interlayer adhesion, on the biomechanical performance of the OCS scaffolds has been extensively studied (Baptista and Guedes, 2021; Berner et al., 2014; Hedayati et al., 2020; Montazerian et al., 2017; Ostrowska et al., 2016; Pierantozzi et al., 2020; Ronca et al., 2016). In addition to OCS scaffolds, lattice structures with other simple unit cells with various pore geometries, such as circular, oval, square, and triangular pores have been studied from mechanical and cell-proliferation perspectives. In addition to the simple unit cells with straightforward pore shapes, more complex unit-cell topologies, usually inspired by natural structures, have also been investigated to enhance the biomechanical behavior of orthopedic scaffolds. For example, triply periodic minimal surface (TPMS) lattice structures are proven to have enhanced fluid permeability (Santos et al., 2020) and mechanical behavior (Castro et al., 2019), which makes them an optimal choice for load-bearing bone scaffolds.

Recently, a group of nature-inspired porous structures have been created based on metallic crystalline structures (Han et al., 2017). A scaffold structure constructed from unit cells with face-centered cubic (FCC) pores was first proposed by Diego et al. (2007). They investigated the effect of geometric characteristics of the pores on the elastic response of this structure, which reports that the compressive elastic behavior of the scaffold is independent of pore size and interconnection throat size but depends only on the porosity of the FCC-based structure. Sanz-Herrera et al. (2008) also investigated the same scaffold architecture from the mechanical, permeability, and specific surface points of view. They concluded that contrary to many conventional scaffold structures, the one based on the FCC arrangement of pores mimics the mechanical and biological properties of bone, which makes it an appropriate choice for bone replacement. The presented FFC scaffold by Diego et al. (2007) and Sanz-Herrera et al. (2008) is a good candidate for a bone scaffold from the mechanical and cell-proliferation perspectives; however, any increase in the porosity of the scaffold, which is usually favorable from the permeability perspective, results in a reduction in the stiffness of the scaffold. The reason for this observation is that the idealized FCC model was based on a cubic unit cell with spherical pores on the corners and in the middle of the faces. Because of this idealization, the mechanical and cell-growth properties of the scaffold depend only on the porosity of the FCC scaffold. Therefore, as a basic concept, a small change in the porosity of the scaffold has a significant effect on its mechanical performance. Therefore, the enhancement of the mechanobiological performance of a porous implant without the change in porosity is the design goal. Accordingly, in an ideal scaffold, increasing the porosity should not compromise the mechanical performance. In this study, in a movement towards this idealization, we propose a new modified scaffold architecture based on the previously introduced FCC unit cells. This new architecture, referred to as MFCC (Modified Face Center Cubic) scaffold, distinguishes between the radii of the spherical pores of the faces and the corners of the FCC unit cell. The introduced architecture gives more degrees of freedom to optimize geometric parameters to reach desired objectives such as enhanced stiffness and permeability. In this study, the geometry of the MFCC scaffold architecture is optimized to maximize the stiffness of the structure under compressive loadings for desired porosities as well as satisfying the cell-growth requirements. Because the mechanical and biological properties of the OCS scaffolds have been studied extensively before, we used this scaffold architecture as a benchmark to evaluate the mechanical performance of the new MFCC scaffolds.

2. Materials and methods

2.1. Scaffold unit cell geometry

FCC unit cells consist of four atoms, which are arranged at the corners and center of each cube face of the cubic cell as follows: eight one-eighth at the corners and six halves in the faces. Similarly, the MFCC model proposed in this study is based on the FCC pores cut from a cube. Fig. 1 shows the 3D structure and the geometrical parameters of the proposed MFCC unit cell. a is the edge length of the unit cell, while r_f and r_c are the radii of spherical pores of the faces and the corners, respectively.

The porosity of the MFCC unit cell can be calculated analytically based on the volumes of the cubic unit cell, the face spheres, and the corner spheres as follows:

$$V_{cube} = a^3 \tag{1}$$

$$V_f = \frac{4}{3}\pi r_f^3 \tag{2}$$

$$V_c = \frac{4}{3}\pi r_c^3 \tag{3}$$

where V_{cube}, V_f, and V_c are the volumes of the cubic unit cell, the spheres on the face center, and the spheres in the corner, respectively. To guarantee the interconnectivity of the pores of the scaffold, the spherical pores on the corners and faces need to intersect. The volume of this intersection should be considered in the porosity calculations. Let S_f and S_c be two intersecting spheres of radii r_f and r_c whose centers are located at $(0,0,0)$ and $(\frac{\sqrt{2}}{2}a,0,0)$, respectively as depicted in Fig. 2(a). The intersection volume, V_{int}, is as follows:

$$V_{int} = \frac{\pi}{6\sqrt{2}a}\left(r_c + r_f - \frac{\sqrt{2}}{2}a\right)^2\left(\frac{a^2}{2} + \sqrt{2}ar_c - 3r_c^2 + \sqrt{2}ar_f + 6r_cr_f - 3r_f^2\right) \tag{4}$$

An MFCC unit cell has six face-centered hemispherical pores in addition to eight one-eighth sphere pores in the corners. Therefore, the overall volume of the pores (V_{pore}) within a cubic MFCC unit cell is as follows:

$$V_{pore} = 3V_f + V_c - 12V_{int} \tag{5}$$

The porosity of scaffold, φ, is the ratio of the total pore volume to the volume of the cubic unit cell and can be expressed in the form of the following:

$$\varphi = \frac{V_{pore}}{V_{cube}} \tag{6}$$

Varying the geometric parameters of the MFCC structure, a range of

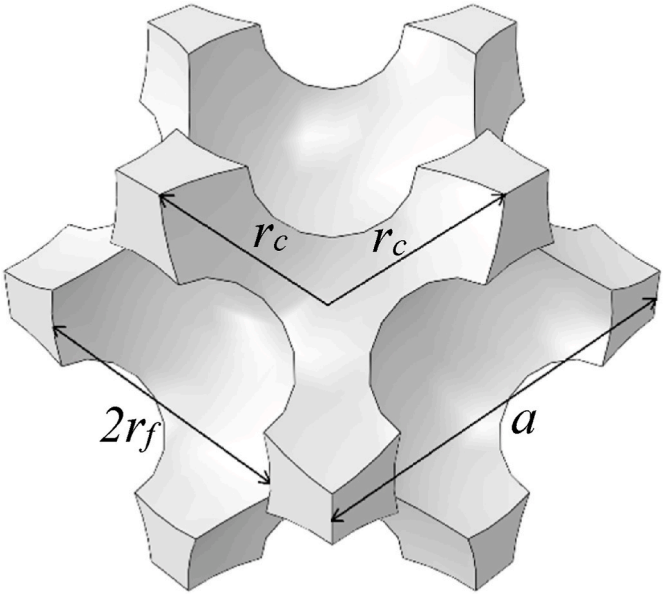

Fig. 1. Geometric characteristics of the proposed MFCC unit cell.

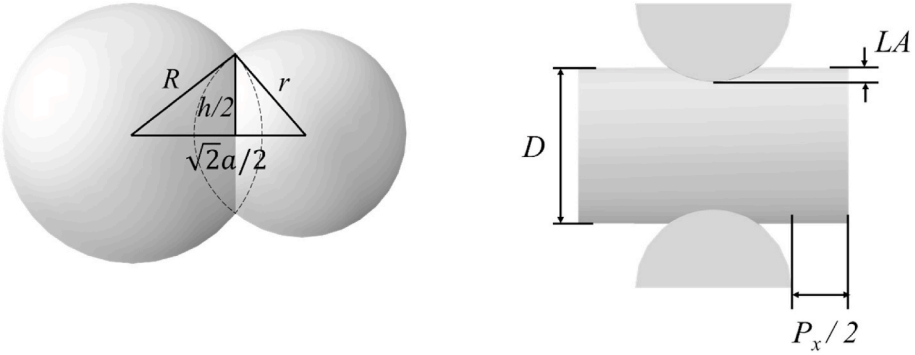

Fig. 2. (a) Intersection of two spheres. (b) Side view of the unit cell of the OCS scaffold.

porosities from 65% to 85% can be reached which is in the proposed range for bone cell proliferation (Abbasi et al., 2020, 2020, 2020; Buj-Corral et al., 2018). In addition to the porosity of the scaffold, pore size is also an essential parameter from cell-growth perspective. As shown in Fig. 2(a), the diameter of the circular pore created at the intersection of spherical pores on the corners and faces of the MFCC unit cell is denoted by h. It can be calculated as a function of r_f and r_c as Eq. (7), where $r = \min(r_f, r_c)$ and $R = \max(r_f, r_c)$. The interconnection throat size, h, in the MFCC scaffold is crucial because it should be large enough to match the cell-proliferation requirements.

$$h = \frac{\sqrt{2}}{a}\sqrt{2a^2R^2 - \left(\frac{a^2}{2} - r^2 + R^2\right)^2} \tag{7}$$

2.2. Optimization problem

In this paper, we implement a numerical approach to optimize the geometrical features of the MFCC scaffold to increase the stiffness of the structure in a predefined porosity. Eq. (8) is utilized to calculate the stiffness of different scaffold structures. The compressive displacement applied to the scaffold results in a reaction force RF on the scaffold. To calculate the effective Young's modulus of the scaffold under this uniaxial compression, the reaction force is converted to stress by dividing it to $A_{mean}=(1-\varphi)A_c$, which is the average cross section area of the scaffold in the planes normal to the compression direction, where A_c is the full cross section area (disregarding the pores) normal to the compression direction. The effective Young's modulus (E_{eff}) of the scaffold is calculated by dividing the stress by the compressive strain ($\varepsilon_0 = \Delta L/ L_0$) as shown in Eq. (8), where ΔL and L_0 are the length change and the initial length of the scaffold in the compression direction.

$$E_{eff} = \frac{RF/A_{mean}}{\varepsilon_0} = \frac{RF/[(1-\varphi)A_c]}{\Delta L/L_0} \tag{8}$$

Throughout this article, E_{eff} is referred to as the "effective Young's modulus" or "apparent stiffness" of scaffold which for simplification is used interchangeably with "stiffness".

The geometry of an MFCC scaffold is determined by its unit cell edge length a, and the radii of spherical pores r_f and r_c. The optimization problem based on these geometrical parameters can be stated as Eq. (9), where $P_{\min}$ and $P_{\max}$ are the recommended minimum and maximum pore sizes based on cell-proliferation requirements. In this study, $P_{\min}$ and $P_{\max}$ are taken to be 400 and 800 μm respectively (Abbasi et al., 2020; Chen et al., 2020; Lee et al., 2019; Murphy et al., 2010; Ouyang et al., 2019; Torres-Sanchez et al., 2017; Zaharin et al., 2018). Considering the mechanobiological requirements of bone scaffolds, geometrical optimization of the MFCC scaffold structure, formulated as Eq. (9), is a constraint-driven problem. Constraints C_1 and C_2 determine the upper and lower bounds of r_f and r_c, respectively. "In the constraints, C_1 and C_2, r_{fmin}, r_{fmax}, r_{cmin}, and r_{cmax} are the lower bound of r_f, the upper bound of r_f, the lower bound of r_c, and the upper bound of r_c, respectively. The lower bounds of r_f and r_c are determined according to the manufacturing limitations. In this study, because the minimums of r_f and r_c are already limited to 400 μm by the constraints C_3 to C_6, any further lower bounds were not applied for r_f and r_c. The upper bound of r_f and r_c is determined by the specific surface area (S_v) of the scaffold structure. A bone mimetic scaffold is expected to have a S_v comparable to the bone tissue of the implantation site. The S_v values reported in the literature for the bones of different regions of human body include a wide range and are subject specific (Lerebours et al., 2015). In this study, the maximum r_f and r_c were chosen to be 1 mm to have an approximate minimum specific surface area of 3 mm^{-1} reported by previous studies (Fyhrie and Kimura, 1999; Lerebours et al., 2015; Martin, 1984) for bone tissues with the considered range of porosities in this study (70%–80%).

Additionally, three more constraints based on the biomechanical requirements of bone scaffolds need to be considered: constraints C_3 and C_4 set an upper limit to the radii of spherical pores, which guarantee the integrity and connectivity of the porous structure, and constraint C_5 which imposes a limit on the size of the pores created in the intersection of the corner and face spheres in the unit cell. Constraint C_3 ensures that the radius of the corner spherical pores (r_c) are smaller than half of the unit cell edge length (a) to guarantee the connectivity of the structure. Constraint C_4 verifies that the radius of spherical pores on the faces (r_f) do not exceed $\frac{\sqrt{2}}{4}a$ to maintain the integrity of the structure. Constraint C_5 ensures that the circular pores, created as the result of intersection of corner and face spheres in the unit cell, are in the recommended pore size range in the literature.

$$\begin{aligned}
&\textit{Maximize} \quad E_{eff}(a, r_f, r_c)\\
&\textit{Subject to} \quad C_1: r_{f\min} < r_f < r_{f\max}\\
&\qquad C_2: r_{c\min} < r_c < r_{c\max}\\
&\qquad C_3: r_c - \frac{a}{2} < 0\\
&\qquad C_4: r_f - \frac{\sqrt{2}}{4}a < 0\\
&\qquad C_5: P_{\min} < h(r_f, r_c) < P_{\max}\\
&\qquad C_6: \varphi = \varphi_0
\end{aligned} \tag{9}$$

The compressive stiffness of porous scaffolds is highly dependent on porosity. A scaffold with a greater porosity tends to have a smaller stiffness. Therefore, topological optimization of a certain scaffold needs to be performed in a constant porosity. Based on Eqs. (1)–(6), the porosity of the scaffold is a function of a, r_f, and r_c. Therefore, a can be extracted for a certain set of φ_0, r_f and r_c and the optimization problem in a constant porosity φ_0 reduces to the following problem with two design parameters r_f and r_c:

$$\begin{aligned} &\textit{Maximize} && E_{eff}(rf, rc) \\ &\textit{Subject to} && C_1: r_{f\min} < r_f < r_{f\max} \\ & && C_2: r_{c\min} < r_c < r_{c\max} \\ & && C_3: r_c - \frac{a(r_f, r_c)}{2} < 0 \\ & && C_4: r_f - \frac{\sqrt{2}}{4} a(r_f, r_c) < 0 \\ & && C_5: P_{\min} < h(r_f, r_c) < P_{\max} \end{aligned} \tag{10}$$

The abovementioned optimization problem is solved for three different porosities, 70%, 75%, and 80%. Discrete sets of independent variables r_f and r_c over the ranges C_1 and C_2 are considered based on the accuracy of the additive manufacturing machine (Kacmarcik et al., 2018). Increment of the discrete variables is selected to be 20 μm according to the printing accuracy of the Ultimaker S3 3D printer used in this study. Additionally, the constraints C_3 to C_5 restrict the feasible region of independent variables r_f and r_c, which further confines the design space.

An exhaustive search optimization approach is used in this study because there is a limited number of feasible solution sets, and the approach has a low finite element computational complexity. Accordingly, the objective function value, E_{eff}, is calculated for all the feasible sets of design parameters (r_f, r_c). This approach gives insights into the effect of the geometrical parameters on the stiffness of the scaffold and meanwhile enables us to find the optimal design without dealing with complicated optimization techniques.

The results of the optimization process are technically independent of the input values for the elastic material properties. Therefore, the E_{eff} reported in the optimization section are normalized using the Young's modulus of the bulk specimen:

$$\overline{E}_{eff} = \frac{E_{eff}}{E_{bulk}} \tag{11}$$

where $\overline{E}_{eff}$ is the normalized effective Young's modulus of the porous scaffold, and E_{bulk} is the Young's modulus of the scaffold material extracted from compression tests of bulk cylindrical Tough PLA specimens. To make the results of this study more comprehensive, the geometric parameters r_f and r_c are also normalized using their maximum values in this study:

$$\overline{r}_f = \frac{r_f}{r_{fmax}} \tag{12}$$

$$\overline{r}_c = \frac{r_c}{r_{cmax}} \tag{13}$$

where $\overline{r}_f$, $\overline{r}_c$, r_{fmax}, r_{cmax} are the normalized radius of face spheres, the normalized radius of corner spheres, the maximum value of r_f, and the maximum value of r_c, respectively.

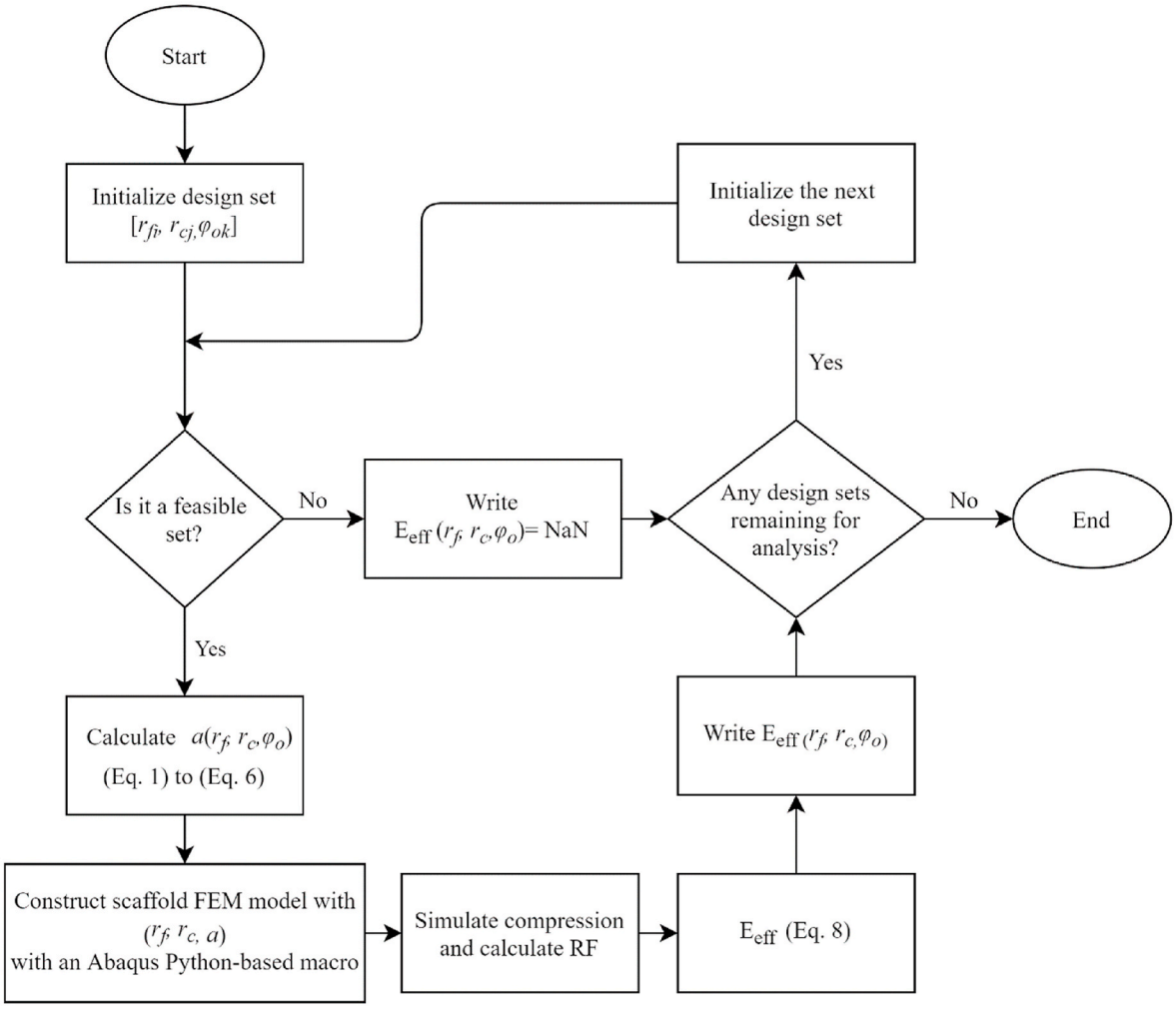

Fig. 3. Flowchart of the optimization process to enhance the stiffness of the MFCC scaffolds.

2.3. Finite element (FE) analysis

Fig. 3 shows a flowchart of the optimization process utilized in this study. The top part of the algorithm depicts the constraint-checking process conducted by MATLAB (MATLAB R2021a, n.d.; MATLAB 2012b), while the bottom section illustrates the FE process, which is carried out by Python scripting in ABAQUS, 2019 (ABAQUS, 2019). The python script receives the feasible set of geometrical parameters (r_f, r_c, a) from MATLAB and creates the 3D FE model of the scaffold based on these parameters. The linear elastic properties of the Tough PLA are extracted from the compression tests of bulk cylindrical Tough PLA specimens, as elaborated in Section 2.6.

The FE model of the scaffold is automatically meshed using a 4-node linear tetrahedral element (C3D4). Fig. 4 shows the scaffold model. To reduce the computational cost of the analysis, five symmetry planes (as shown in Fig. 4), are considered. A rigid plane is modeled to apply the compressive displacement. The applied compressive strain is small enough to ensure that the stresses and strains of the whole scaffold remain in the elastic region. A hard contact with penalty friction with a coefficient of 0.2 (Aziz et al., 2020; Hanon et al., 2019) is assumed between the scaffold and the rigid plate. A mesh sensitivity analysis is conducted to reach an optimum number of elements in the models that considers the accuracy requirements. The implemented parameters in the FE analysis are summarized in Table 1.

2.4. Fabrication of samples

To characterize the compressive mechanical properties of tough PLA, standard compression samples were fabricated by an FDM machine (Ultimaker S3) using Ultimaker Tough PLA Black filament. The CAD models created in ABAQUS are exported in STL file format and then converted to ufp files by Ultimaker Cura. The printable ufp files, which contain the specific information regarding geometry of the parts and the printing parameters, are imported to the printing device. The standard compressive test specimen recommended by ASTM D695 is 3D-printed in the form of a right cylinder with the aspect ratio of $h/D = 2$ (25.4 mm height and 12.7 mm diameter). The same method is used to fabricate porous scaffold specimens. It should be noted that the material properties of polymeric materials are highly dependent on printing parameters (Garzon-Hernandez et al., 2020; Mazzanti et al., 2019).

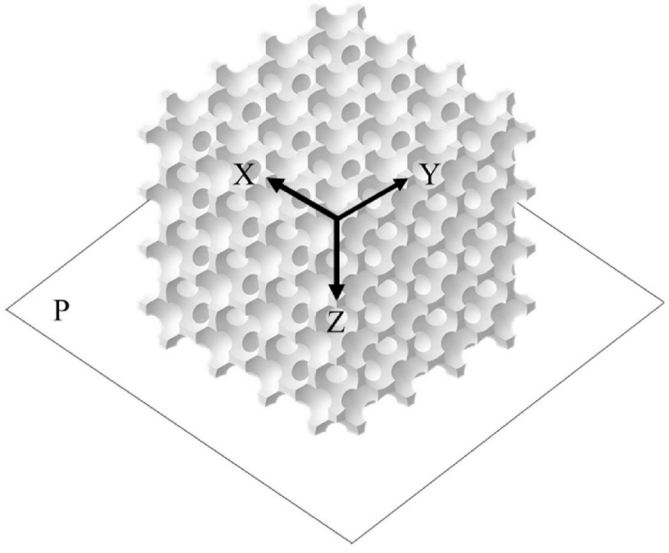

Fig. 4. A scaffold model and the compression rigid plate P. Five symmetric boundary conditions are defined on the model: XY plane, YZ plane, XZ plane, and the two perpendicular planes behind the scaffold (not visible in the isometric view) parallel to YZ and XZ planes. The mesh of the FE model is hidden to better visualize the scaffold geometry.

Table 1
FE analysis parameters.

Description	Value
Studied porosities	70%, 75%, 80%
Minimum pore size (P_{min})	400 μm
Maximum pore size (P_{max})	800 μm
Exhaustive search increment	20 μm
Young's modulus of the bulk specimen	2.353 GPa
Poisson's ratio	0.3
Applied compressive strain (FEM)	0.25%
Penalty friction coefficient	0.2
FEM element type	C3D4

Therefore, all cylindrical bulk specimens and porous scaffolds were fabricated with the same printing parameters as mentioned in Table 2. To reduce the effect of manufacturing parameters, scaffolds were printed triple scaled.

2.5. Comparison of MFCC and OCS scaffolds

Most of the research in the field of scaffold design has been done on lattice structures built from orthogonal cylindrical struts (OCS scaffolds). Therefore, OCS scaffolds are good benchmarks to evaluate new porous scaffold structures such as MFCC. We analytically formulated the porosity of the OCS scaffolds to compare MFCC scaffolds with OCS scaffolds of the same porosity. Fig. 2(b) shows the unit cell of the OCS scaffold which consists of cylindrical struts with diameter D, and a layer adhesion of LA. The pore size in the x and z directions is assumed to be the same and equal to P_x. From the general formula of porosity in Eq. (6), we have $\varphi = 1 - V_s/V_{cube}$, where $V_{cube} = 2(D-LA)(D+P_x)^2$ is the volume of the unit cuboid and $V_s = (\pi D^2/2)(D+P_x) - 2V_{int}$ is the volume of the cylindrical struts of the scaffold. V_{int} is the volume of the intersection of two cylinders:

$$V_{int} = \frac{2}{3}D^3[(2-m)E(m) - 2(1-m)K(m)] \tag{14}$$

where $m = sin^2(t_0)$, and $t_0 = cos^{-1}[(D - LA)/D]$. $E(m)$ and $K(m)$ are complete elliptic integrals of first and second kind, respectively. Substituting these parameters in Eq. (6), the porosity of the OCS scaffolds is derived as follows:

$$\varphi = 1 - \frac{(\pi D^2/2)(D+P_x) - (4D^3/3)[(2-m)E(m) - 2(1-m)K(m)]}{2(D-LA)(D+P_x)^2} \tag{15}$$

OCS structures of the porosities 70%, 75%, and 80% are designed and implemented in Abaqus software. An FE simulation of the scaffold compression has been performed on OCS scaffold structures. The results are compared to those of MFCC design in similar porosities to investigate the effect of geometrical parameters on the scaffold stiffness. To quantitively compare the stiffness of OCS and MFCC scaffolds, the stiffness percentage change is defined as the ratio of difference between the two stiffnesses to the stiffness of OCS scaffold:

$$\Delta E\% = \frac{|E_{MFCC} - E_{OCS}|}{E_{OCS}} \times 100\% \tag{16}$$

Table 2
Printing parameters.

Printing parameter	Value
Nozzle Temperature	205 °C
Build Plate Temperature	60 °C
Infill Density	100%
Infill Pattern	Lines
Print Speed	50 mm/s
Nozzle Diameter	250 μm
Layer Height	100 μm
Filament Diameter	2.85 mm

where $\Delta E\%$ represents the percentage change of the stiffness and E_{MFCC} and E_{OCS} are the stiffnesses of MFCC and OCS scaffolds, respectively.

2.6. Compression tests

The compression tests were conducted on a Shimadzu AGS-X (50 kN, Table-top Model) universal testing machine based on ASTM D695 (D20 Committee,) to evaluate the compressive Young's modulus of the Tough PLA material. The bulk cylindrical specimens described in Section 2.4 were compressed and their stress-strain curves were extracted. The elastic modulus of the bulk material was calculated using the slope of the initial linear region of the curve.

The same approach was used to evaluate the compressive behavior of porous scaffolds under compression. To validate the results of FE simulations, the E_{eff} values extracted from Abaqus were compared to the experimental results. MFCC and OCS scaffolds were tested with porosities of 70%, 75%, and 80%. Scaffolds were slowly compressed to 20% strain with the rate of 0.002 1/s to avoid the effect of the strain rate-dependent behavior. The reaction force-displacement diagrams were extracted from the test machine and converted to the equivalent stress-strain diagrams. The slope of the stress-strain diagram is defined as the effective Young's modulus of the scaffold, E_{eff}. Three samples for each test were fabricated and the reported results are an average of triplicate measurements.

The yielding behavior of the MFCC scaffold is also compared to OCS structures. Determining a yield point for a structure is not straightforward, because different regions do not yield simultaneously. In this study, the lowest stress point at which nonlinearity occurs is defined as apparent yield strength of the scaffold and is denoted by Y.

3. Results

The results of optimization, FE simulation, and compression tests of the new MFCC scaffolds are presented and discussed in this section. The mechanical performance of the MFCC design is also numerically and experimentally compared to the regular OCS scaffolds of the same porosity.

3.1. Feasible design space

The stiffness of the MFCC scaffold in a predefined porosity depends on the geometrical variables $\bar{r}_f$ and $\bar{r}_c$. To maximize this stiffness, the feasible regions of the independent variables $\bar{r}_f$ and $\bar{r}_c$ are extracted according to the structural and biological constraints mentioned in Section 2.2. As shown in Fig. 5, for each constraint, the yellow and blue regions of the diagrams show the feasible and infeasible design sets, respectively. The last row of the diagram is the overlap of constraints C_3, C_4, and C_5, which demonstrates the final feasible design space for each porosity.

As shown in Fig. 5, the total number of feasible design sets is limited. This is due to two main reasons: first, the scaffold design problem has a highly constrained nature, and second, the continuous design space is discretized based on the accuracy of the 3D printing device. Specifically, assuming the accuracy of the printer utilized in this study (Ultimaker S3) to be 20 μm (Kacmarcik et al., 2018), $P_{\min} = 400$ μm, and $P_{\max} = 800$ μm, the numbers of feasible sets of parameters (r_f, r_c) are 111, 177, and 116 for φ_0 =70%, φ_0 =75%, *and* φ_0 =80%, respectively, which totals 404 feasible design sets to be solved by FE method.

3.2. Optimized MFCC scaffold

Fig. 6 shows the normalized effective Young's modulus ($\overline{E}_{eff}$) of the MFCC scaffolds for all the feasible design sets ($\bar{r}_f$, $\bar{r}_c$). The three surfaces in Fig. 6(a) correspond to the three porosities 70%, 75%, and 80%. As elaborated in Section 3.1, the design sets that violate the cell growth requirements are discarded as infeasible sets. Therefore, all of the designs shown in Fig. 6 satisfy the cell-growth requirements.

As demonstrated in Fig. 6(a), the stiffness of scaffolds increases when porosity decreases. Comparing the optimum designs of the two porosities 80% and 70%, a decrease in porosity from 80% to 70%, results in a 41.4% drop of the scaffold stiffness. In addition to scaffold porosity, geometrical parameters ($\bar{r}_f$, $\bar{r}_c$) affect the stiffness of the scaffold. Two-dimensional representations of the surfaces shown in Fig. 6(a) are presented separately for the three different scaffold porosities in Fig. 6(b), (c), and (d). In a constant porosity of 70%, as shown in Fig. 6(b), an optimum choice of geometric features ($\bar{r}_f = 0.8$, $\bar{r}_c = 1$) results in a structure with a normalized stiffness of 0.39 (point A), while a non-optimum choice of these parameters ($\bar{r}_f = 0.5$, $\bar{r}_c = 0.86$) gives a 6.3% lower stiffness, which is a non-optimal design (point D). Therefore, using the same amount of material and simply by varying the geometry of the scaffold, a higher stiffness can be achieved. Similar to the porosity of 70%, the optimal and non-optimal design points of the porosities 75% and 80% are shown on Fig. 6(c) and (d).

3.3. Comparison of optimal MFCC, non-optimal MFCC, and OSC scaffolds

To better illustrate the effect of geometrical parameters r_f, r_c, and scaffold porosity on the distribution of loads in the structure of the scaffolds, CAD models of the optimized scaffolds with porosities 70%, 75%, and 80% are compared with three non-optimal designs of the same porosities in Fig. 7 (a)–(f). From Fig. 6, the points A, B, and C correspond to the optimal design parameters, while points D, E, and F are three sets of parameters in the feasible design space, which yields non-optimal scaffold structures. The design parameters of the scaffolds are also mentioned in Fig. 7. The maximum von Mises stress of each scaffold is shown in Fig. 7. The results of the mesh convergence analysis are presented in Supplementary Materials. A comparison of the optimal and non-optimal designs for all porosities reveals that the optimal designs have a lower maximum stress compared to the non-optimal designs of the same porosity. Stress concentration happens in the interconnection throat regions, as indicated in Fig. 7(d), (e), and (f).

Regular lattice scaffolds with OCS structures are designed and compared to the MFCC structure proposed in this study. Fig. 7 compares the FE contours of the two designs under 0.25% compressive strain. Comparing the von Mises contours of the two designs, the MFCC scaffolds maintain a more efficient distribution of loads through the scaffold structure compared to the OCS scaffolds. In the same porosity, the OCS design has a lower E_{eff} compared to the MFCC scaffold. Even non-optimal MFCC scaffolds have greater stiffness than the OCS scaffolds at the same porosity. For all the porosities, MFCC scaffolds have a lower maximum stress compared to the OCS scaffolds.

3.4. Verification of the finite element method (FEM) results with experimental results

To validate the FEM results, three optimum designs of MFCC and three OCS scaffolds of the same porosity were fabricated by FDM. The standard compressive test was performed on all samples and the engineering stress-strain curves are presented in Fig. 8. The curves consist of an initial linear region, followed by a nonlinear behavior beyond an approximately 2.5% engineering strain. As expected, MFCC scaffolds shows a greater stiffness compared to OCS scaffolds. Beyond the yielding point, MFCC and OCS scaffolds show a different behavior. OCS scaffolds show strain hardening behavior beyond the linear region, which exhibits an approximately bilinear stress-strain curve in the tested strain range, while MFCC scaffolds show a strain-softening behavior immediately after the linear region followed by some oscillations related to local delamination and regional yielding of the scaffold structure. A qualitative comparison of the curves of Fig. 8 shows that for both scaffold types,

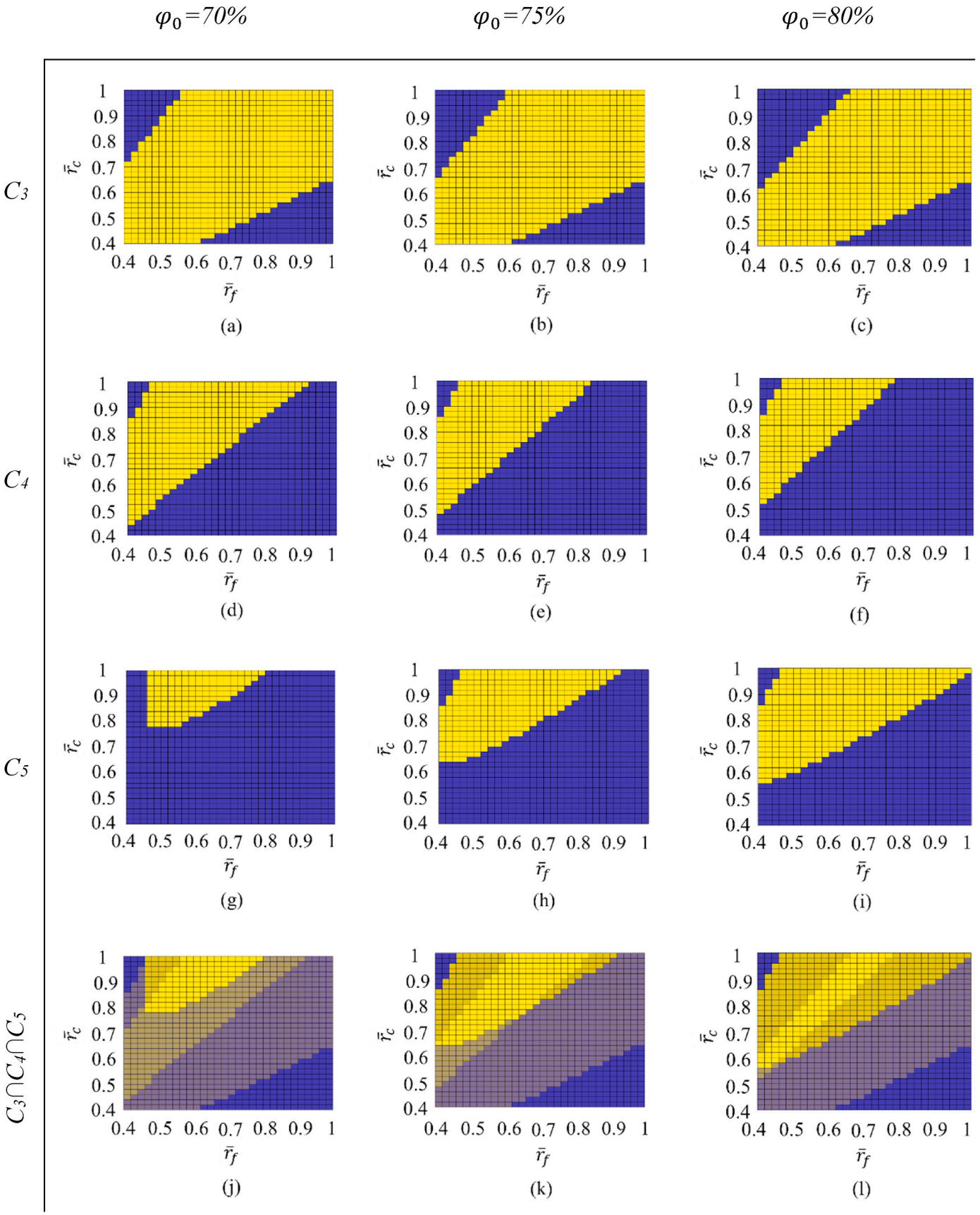

Fig. 5. The feasible region of independent variables r_f and r_c based on the constraints C_3, C_4 and C_5. (a) to (i) show the feasible design sets marked in yellow and the infeasible sets marked in blue. (j), (k), and (l) show the overlap of C_3, C_4, and C_5 constraints with different transparencies, in which the yellow region is the final feasible area as the overlapping area of the three constraints.

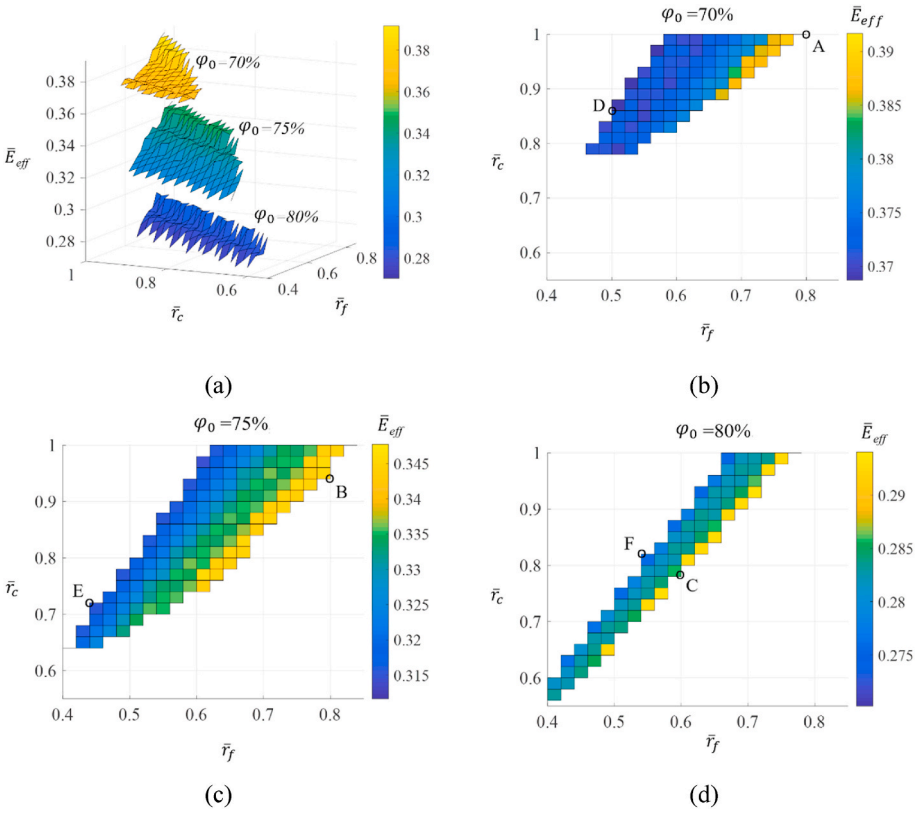

Fig. 6. Variation of normalized effective Young's modulus, $\bar{E}_{eff}$, with geometrical parameters $\bar{r}_f$ and $\bar{r}_c$. (a) comparison of $\bar{E}_{eff}$ of the three different porosities 70%, 75%, and 80%; (b) $\varphi_0 = 70\%$; (c) $\varphi_0 = 75\%$, and (d) $\varphi_0 = 80\%$.

there is a drop in the slope of the initial linear region of the curves (apparent stiffness of the scaffold) when porosity increases. Furthermore, the scaffold with a greater porosity has a lower level of the stress at the onset of yielding. The comparison of the MFCC scaffold curves with those of the OCS structure indicates that in a predefined porosity, the MFCC scaffold has a stiffer structure as well as a greater stress at the yielding onset.

A quantitative comparison of the stiffness and yielding onset of the stress-strain curves of Fig. 8 is presented in Fig. 9. The effective Young's modulus (E_{eff}) and apparent yield point (Y) of the experimental curves are extracted from the Fig. 8 and summarized in Fig. 9. Fig. 9(a) compares the experimental and FEM effective Young's moduli for MFCC and OCS scaffolds. Based on the experimental results in Fig. 9(a), MFCC scaffolds with 70%, 75%, and 80% porosities are 39.2%, 37.1%, and 10.0% stiffer, respectively, compared to OCS scaffolds with the same porosities. The apparent yield point of the scaffolds is compared in Fig. 9 (b). The MFCC scaffolds with porosities 70%, 75%, and 80% have 60.4%, 74.7%, and 48.6% greater apparent yield points, respectively, compared to the OCS scaffolds. As shown in Fig. 9(a), the predicted E_{eff} by the FEM agree with the experimental results.

Table 3 lists the percentage of discrepancy between the test results and the FEM predictions. The FEM predictions are accurate for MFCC and OCS scaffolds in all porosities except MFCC at 80% porosity. The reason for this discrepancy is discussed in the Discussions section.

The fabricated MFCC and OCS scaffolds with 70% porosity specimens are shown in Fig. 10(a) and (b). Fig. 10 includes isometric views, side views before compression, and side views after 10% compression. Both designed scaffolds have overhang features that usually reduce the quality and accuracy of the print. In this study, the printing parameters are optimized to reduce the negative effects of these overhangs on the print quality, as shown in Fig. 10 (a)–(d). As shown in Fig. 10(e), the MFCC scaffold under compression exhibits delamination in the outer surface of the scaffold (region R_5 and similar delaminated regions in Fig. 10(e)). The trace of this delamination is clearly observed in Fig. 8, where the stress-strain curves of the MFCC scaffolds exhibit strain softening at regions beyond 10% compression. As shown in Fig. 8, in the comparison of MFCC scaffolds with different porosities, the scaffold with a lower porosity (70%) exhibits fewer oscillations in the stress-strain curve compared to more porous MFCC scaffolds (80%). This is associated with the smaller features of the scaffolds with a greater porosity, which results in an easier delamination and local buckling under compression. Contrarily, as shown in Fig. 10(f), due to their regular structure, OCS scaffolds do not exhibit any sign of delamination or local buckling. This is also reflected in the stress-strain curves of OCS scaffolds in Fig. 8. Unlike the stress-strain curves of the MFCC structure, OCS scaffolds exhibit stable post-yielding stiffness with no oscillations. It is worth mentioning that although we performed the compression tests under large strains to observe the failure mechanism of the scaffolds, the scaffolds should be designed so that the structure works in the elastic region. In the elastic region as the favorable working zone, the MFCC scaffolds have multiple advantages over OCS scaffolds.

The obtained optimal design parameters are summarized in Table 4. The last row of the table contains the percentage change from the stiffness of the OCS scaffolds to the stiffness of the optimal MFCC scaffold with the same porosity. The enhancement in the stiffness of the scaffold in Table 4 is shape attributed and is independent of the material used. Therefore, the same percentage increase in the stiffness is achievable for a broad range of materials.

4. Discussions

Architecture of a porous scaffolds significantly influences both the mechanical and cell-growth performance of the scaffold. Therefore, optimization of the geometry of the scaffold should be considered during the design procedure. The shape optimization method utilized in this study is based on an exhaustive search among the feasible design sets

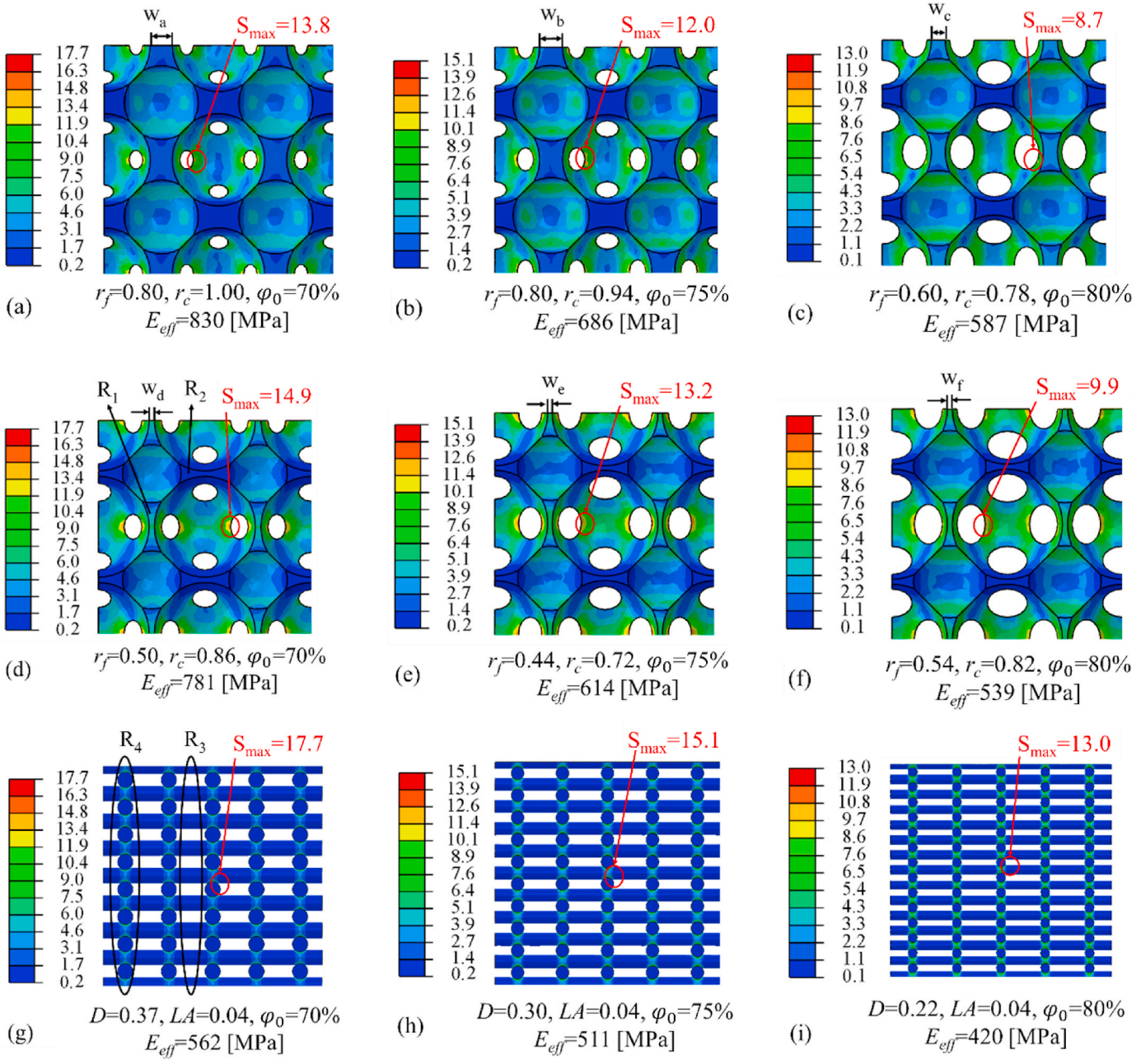

Fig. 7. Side view of von Mises stress contours of optimal MFCC, non-optimal MFCC, and OCS scaffold geometries under 0.25% uniaxial compressive strain in the vertical direction. (a), (b), and (c) are optimal designs for φ_0 =70%, φ_0 =75%, and φ_0 =80%, respectively. (d), (e), and (f) are non-optimal designs for φ_0 =70%, φ_0 =75%, and φ_0 =80%, respectively. (g), (h), and (i) are non-optimal designs for φ_0 =70%, φ_0 =75%, and φ_0 =80%, respectively. D and LA are the strut diameter and layer adhesion of the OCS scaffolds, respectively. S_{max} is the maximum von Mises stress. Stress unit is [MPa]. Dimensions r_f, r_c, D, and LA are in mm.

and can be modified for optimization of any porous structure. If the number of feasible design sets was much more than what we had in this study, the exhaustive search method would consume time and resources and it would be preferable to employ metaheuristic optimization methods such as genetic algorithm.

In comparison of the MFCC structure to the regular OCS scaffolds with the same porosity, as shown in Figs. 7 and 9, the MFCC structure is superior to the OCS design from three distinct perspectives: 1) stiffness; 2) stress concentration; and 3) cell-proliferation rate. As far as the stiffness of the structure is concerned, the MFCC design outperforms the OCS design and achieves 48%, 34%, and 40% stiffer structure with porosities 70%, 75%, and 80%, respectively, as summarized in Table 4. This is due to the gradual variation of the cross-section in the MFCC structure which provides distribution of the applied compressive load to the entire structure of the scaffold. Contrarily, the low stress levels of the horizontal connections of the OCS structure (region R_3 in Fig. 7(g) and similar horizontal connections in Fig. 7(h) and (i)) show that these horizontal connections carry a negligible load compared to the high-stress vertical pillars parallel to the loading direction (region R_4 in Fig. 7(g) and similar strut intersection regions in Fig. 7(h) and (i)). In the same porosity, this non-optimal distribution of loads in the OCS design results in a lower E_{eff} in the OCS regular lattice compared to the MFCC scaffold. The similar stress distributions are observed in previous FE simulations on OCS structures, such as the work done by Entezari et al. (2016), which puts emphasis on the load-bearing role of vertical pillars of the OCS scaffolds.

From a stress concentration perspective, as shown in Fig. 7, OCS scaffolds have a greater maximum stress compared to MFCC scaffolds for

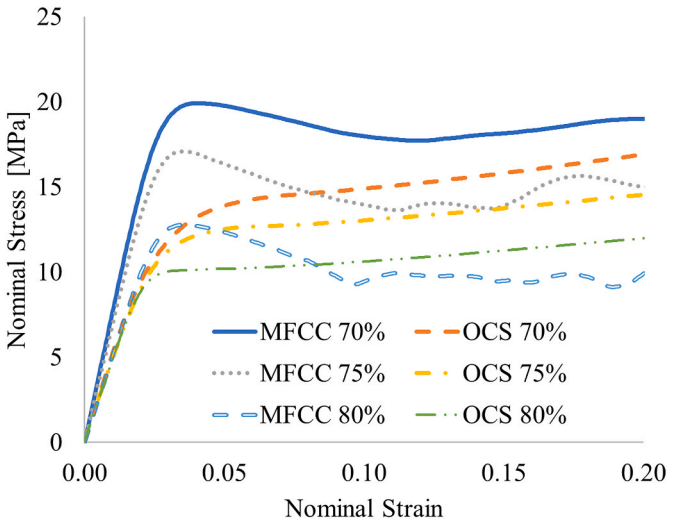

Fig. 8. Experimental stress-strain curves of compression tests of MFCC and OCS scaffolds. Results are reported for three scaffold porosities, 70%, 75%, and 80%.

all the porosities. As demonstrated in Fig. 7(g), (h), and (i), the maximum von Mises stress of OCS structures occurs in the intersection of the orthogonal cylindrical struts. Such a sudden geometric change can potentially lead to the stress concentration. Conversely, the maximum von Mises stress of MFCC scaffolds is lower due to the smooth geometric transitions of its structure through spherical pores. A lower stress level would increase the fatigue life of the MFCC structure (Gomez-Gras et al., 2018), which is essential for bone scaffolds subjected to dynamic loads after implantation.

From the cell-proliferation perspective, MFCC scaffolds are expected to have a better proliferation ability compared to the OCS scaffolds. Past studies show that cell proliferation rate has a direct relationship to curvature, and is larger on concave surfaces compared to planar and convex surfaces (Bidan et al., 2013; Knychala et al., 2013; Rumpler et al., 2008). Therefore, MFCC scaffolds with concave spherical pore shapes are theoretically expected to have a larger cell-proliferation rates compared to OCS scaffolds with convex cylindrical struts.

The FEM results of this study accurately predict the E_{eff} of the scaffolds as shown in Fig. 9(a) and Table 3. The greatest discrepancy is observed in the MFCC scaffold with 80% porosity, with the FEM giving a 26% greater E_{eff} than that obtained from the experiment. This discrepancy is largely due to the manufacturing deviations of the 80% MFCC scaffold, which has not been considered in the idealized FE simulation. The large pores of the MFCC scaffold with 80% porosity leads to smaller feature sizes in comparison to the scaffolds with a lower porosity. The layer-by-layer nature of the fabrication method utilized in this study results in inaccurate 3D-printing of these small features. This issue can be addressed by any other accurate method of fabrication.

There is a geometric distinction between the optimal and non-optimal MFCC designs. For a particular porosity, the width of the vertical pillars of the optimal designs (indicated as w_a, w_b, and w_c in Fig. 7) is wider than this feature of the non-optimal designs (w_d, w_e, and w_f in Fig. 7). Stress distributions in the structures show that these vertical pillars (such as region R_1 in Fig. 7(d)) have a greater von Mises stress compared to the horizontal pillars (such as region R_2 in Fig. 7(d)). This is largely due to the fact that the vertical pillars are parallel to the compression direction and a considerable amount of the external load is applied to these vertical sections rather than the horizontal ones. This phenomenon was also observed in a previous study by Entezari et al. (2016) on the yielding behavior of regular lattice structures. This paper, by assuming a modified face-centered cubic arrangement of pores (MFCC) and utilizing a FEM-based shape optimization, enables us to enhance the mechanical performance of the scaffold without compromising the cell migration requirements. Past efforts have shown that to increase the stiffness of a porous scaffold, the porosity of the structure typically should be reduced (Lin et al., 2004; Poh et al., 2019; Sudarmadji et al., 2011; Zhang et al., 2020). The power relation between the

Table 3
Discrepancy between the experimental and FEM predictions for the MFCC and OCS scaffolds.

Scaffold Type	Scaffold Porosity		
	70%	75%	80%
MFCC	3.3%	0.1%	26%
OCS	2.6%	2.4%	0.9%

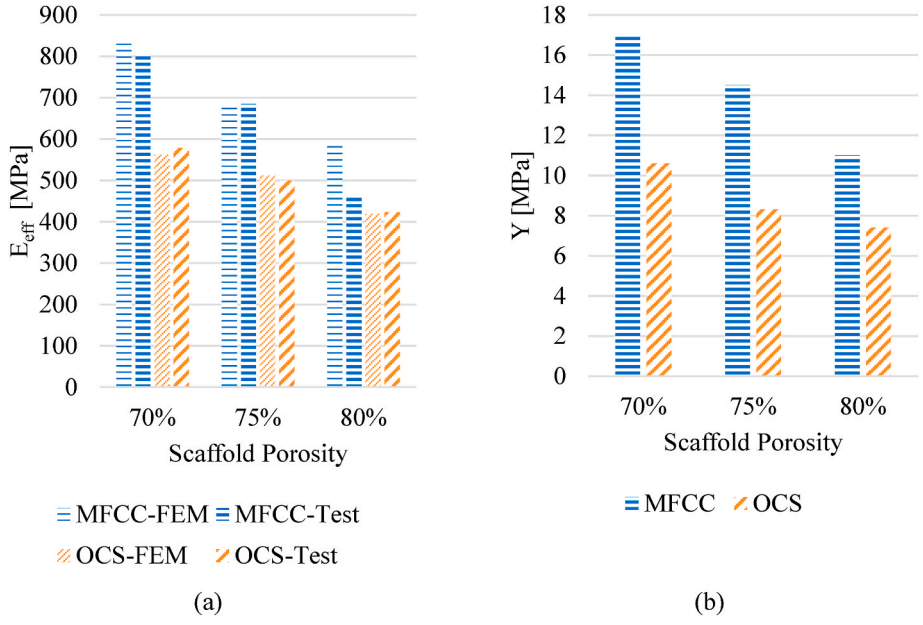

Fig. 9. Comparison of MFCC and OCS scaffolds of porosities 70%, 75%, and 80%. Comparison of (a) experimental and FEM effective Young's moduli, E_{eff}, and (b) apparent yield points, Y.

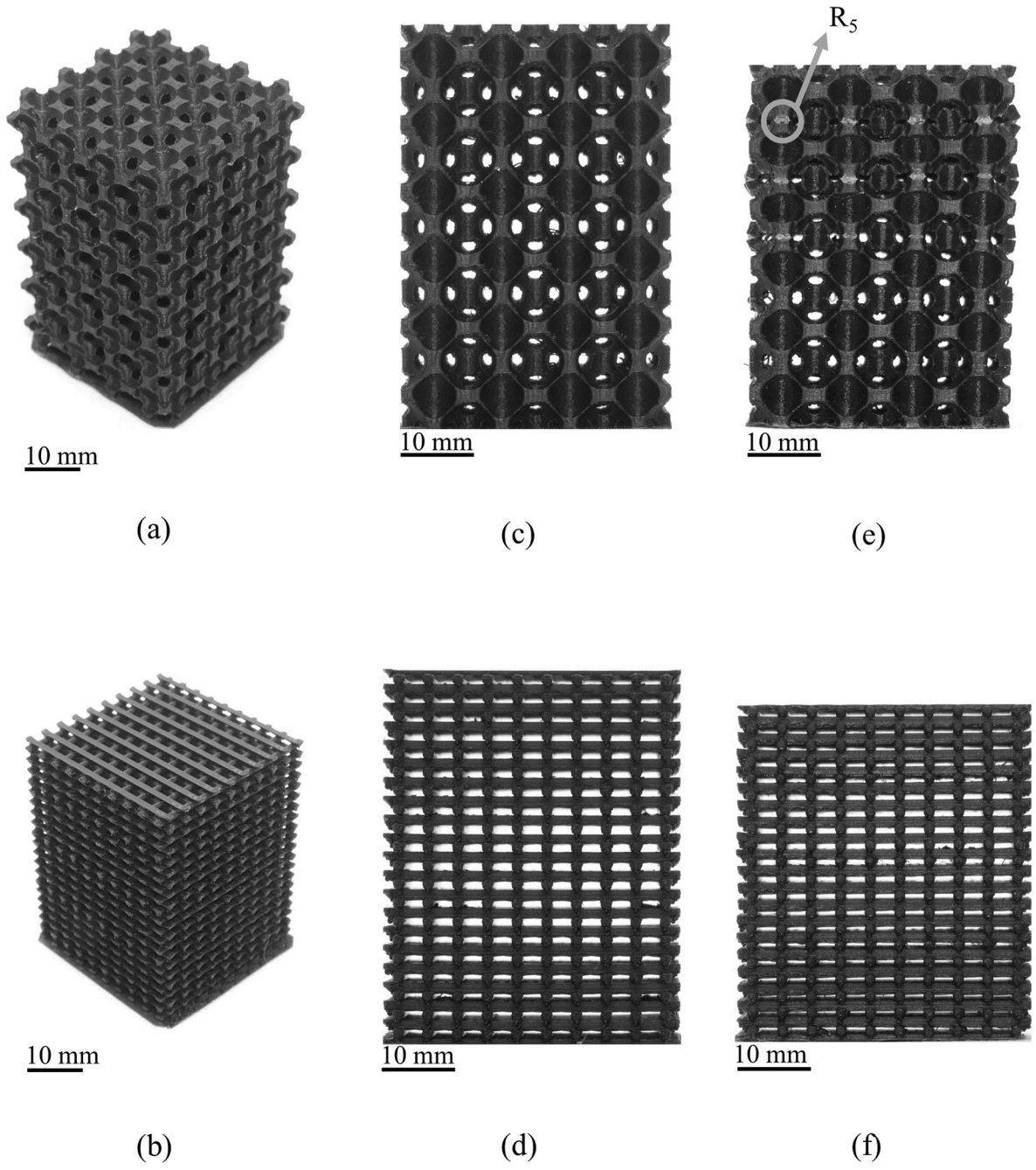

Fig. 10. 3D-printed MFCC and OCS scaffolds with 70% porosity. Isometric view of (a) MFCC, and (b) OCS. Side view before compression of (c) MFCC, and (d) OCS. Side view after 10% compressive strain of (e) MFCC, and (f) OCS.

Table 4
Optimal geometric parameters of the MFCC scaffold and comparison of its stiffness with the OCS scaffold. The stiffness values are FE analysis results.

	Scaffold Porosity		
	70%	75%	80%
r_f [mm]	0.80	0.80	0.60
r_c [mm]	1.00	0.94	0.78
a [mm]	2.47	2.36	1.78
E_{MFCC} [MPa]	830	686	587
E_{OCS} [MPa]	562	511	420
ΔE%	48%	34%	40%

scaffold stiffness ($\bar{E}_{eff}$) and porosity (φ) is well-established as $\bar{E}_{eff} = C(1-\varphi)^2$, where C is a constant dependent on the geometry of the pore (Diego et al., 2007). The inverse relation between the porosity and stiffness of the scaffold is reasonable because scaffolds with a lower porosity in a certain bulk volume have more material compared to the ones with higher porosities. This extra material creates a resistance to the applied external forces, which results in an increase of the stiffness. Furthermore, a reduced porosity usually results in a lower permeability (Bogu et al., 2019; Dias et al., 2012; Lu et al., 2020; Pires et al., 2021) which is unfavorable from cell migration and cell in-growth perspective (Lu et al., 2020; Van Bael et al., 2012). In a step towards the ideal case of increasing the stiffness of the scaffold without having to trade-off the porosity, we optimized the MFCC scaffold geometry in constant porosities, 70%, 75%, and 80%. Results in Fig. 6(a) and Table 4 show that by

selection of the optimal geometrical parameters for the scaffold, we are able to increase the stiffness without having to decrease the porosity. MFCC scaffolds can be utilized in locations such as femur, tibia, and fibula instead of regular OCS scaffolds (Cohen et al., 2017; Ghouse et al., 2019). The approach of our study would provide the basis to design improved scaffolds from both mechanical and biological viewpoints.

5. Conclusion

In this study, a new porous structure based on FCC arrangement of pores (called an MFCC scaffold) was proposed and optimized to enhance the stiffness of the scaffold. To do so, FEM was utilized in combination with an exhaustive search optimization method to find the optimum geometry of the scaffold in a predefined porosity and in consideration of the cell proliferation requirements. The stiffness of the MFCC scaffold was compared with orthogonal cylindrical struts (OCS) scaffolds of the same porosity. FEM results were validated by the corresponding compression tests on the scaffolds fabricated by FDM. The summary of the results is as follows:

- In addition to the porosity, the internal architecture of the MFCC scaffolds influences their stiffness. The size of the spherical pores (r_f and r_c) as well as the unit cell size a influence the stiffness of the MFCC scaffold. The scaffolds with the combinations of r_f and r_c that result in a wider vertical pillar (e.g. w_a), are stiffer.
- For porosities of 70%, 75%, and 80%, the effective Young's moduli of the MFCC scaffolds are 48%, 34%, and 40% larger than those of the OCS scaffolds of the same porosity, respectively.
- For porosities of 70%, 75%, and 80%, the apparent yield points of the MFCC scaffolds are 60.4%, 74.7%, and 48.6% larger than those of the OCS scaffolds of the same porosity, respectively.
- By application of 0.25% uniaxial compressive strain to the scaffolds of porosities 70%, 75%, and 80%, the maximum von Mises stress of the MFCC scaffolds is 22.0%, 20.5%, and 33.1% less than those of the OCS scaffolds of the same porosity, respectively.
- The increase in the stiffness of the scaffolds was achieved only by the architecture optimization which was independent of the implemented material model. Therefore, it is expected that scaffolds manufactured with a different linear elastic material show the same percentage of stiffness increase.

Future studies include consideration of scaffold permeability as an optimization objective and performing a two-objective optimization to design a porous structure that has an optimum stiffness and permeability at the same time.

CRediT authorship contribution statement

Ali H. Foroughi: Writing – original draft, Visualization, Methodology, Investigation, Formal analysis, Data curation, Conceptualization. **Mir Jalil Razavi:** Writing – review & editing, Validation, Supervision, Resources, Project administration, Funding acquisition, Conceptualization.

Declaration of competing interest

The authors declare that they have no known competing financial interests or personal relationships that could have appeared to influence the work reported in this paper.

Acknowledgments

The authors thank Dr. Fuda Ning and Dayue Jiang from the Advanced Materials and Additive Manufacturing (AM2) Lab for assisting in mechanical tests.

Appendix A. Supplementary data

Supplementary data to this article can be found online at https://doi.org/10.1016/j.jmbbm.2022.105098.

References

ABAQUS, 2019. Dassault Systèmes Simulia Corp. Johnston, RI, USA.
Abbasi, N., Hamlet, S., Love, R.M., Nguyen, N.-T., 2020. Porous scaffolds for bone regeneration. J. Sci.: Adv. Mater. Dev. 5, 1–9. https://doi.org/10.1016/j.jsamd.2020.01.007.
Alomari, A.H., Wille, M.-L., Langton, C.M., 2018. Bone volume fraction and structural parameters for estimation of mechanical stiffness and failure load of human cancellous bone samples; in-vitro comparison of ultrasound transit time spectroscopy and X-ray μCT. Bone 107, 145–153. https://doi.org/10.1016/j.bone.2017.11.021.
Ambu, R., Morabito, A.E., 2018. Porous scaffold design based on minimal surfaces: development and assessment of variable architectures. Symmetry 10, 361. https://doi.org/10.3390/sym10090361.
Amini, A.R., Laurencin, C.T., Nukavarapu, S.P., 2012. Bone tissue engineering: recent advances and challenges. Crit. Rev. Biomed. Eng. 40, 363–408.
Standard test method for compressive properties of rigid plastics, 2010.
Aziz, R., Ul Haq, M.I., Raina, A., 2020. Effect of surface texturing on friction behaviour of 3D printed polylactic acid (PLA). Polym. Test. 85, 106434 https://doi.org/10.1016/j.polymertesting.2020.106434.
Baptista, R., Guedes, M., 2021. Morphological and mechanical characterization of 3D printed PLA scaffolds with controlled porosity for trabecular bone tissue replacement. Mater. Sci. Eng. C 118, 111528. https://doi.org/10.1016/j.msec.2020.111528.
Baptista, R., Guedes, M., Pereira, M.F.C., Maurício, A., Carrelo, H., Cidade, T., 2020. On the effect of design and fabrication parameters on mechanical performance of 3D printed PLA scaffolds. Bioprinting 20, e00096. https://doi.org/10.1016/j.bprint.2020.e00096.
Behl, M., Razzaq, M.Y., Mazurek-Budzyńska, M., Lendlein, A., 2020. Polyetheresterurethane based porous scaffolds with tailorable architectures by supercritical CO2 foaming. MRS Advances 5, 2317–2330. https://doi.org/10.1557/adv.2020.345.
Berner, A., Woodruff, M.A., Lam, C.X.F., Arafat, M.T., Saifzadeh, S., Steck, R., Ren, J., Nerlich, M., Ekaputra, A.K., Gibson, I., Hutmacher, D.W., 2014. Effects of scaffold architecture on cranial bone healing. Int. J. Oral Maxillofac. Surg. 43, 506–513. https://doi.org/10.1016/j.ijom.2013.05.008.
Bidan, C.M., Kommareddy, K.P., Rumpler, M., Kollmannsberger, P., Fratzl, P., Dunlop, J.W.C., 2013. Geometry as a factor for tissue growth: towards shape optimization of tissue engineering scaffolds. Adv. Healthc. Mater. 2, 186–194. https://doi.org/10.1002/adhm.201200159.
Bogu, V.P., Madhu, M.N., Kumar, Y.R., Kumar, K.A., 2019. Design and analysis of various homogeneous interconnected scaffold structures for trabecular bone. In: Mechanical Engineering for Sustainable Development. Apple Academic Press.
Buj-Corral, I., Bagheri, A., Petit-Rojo, O., 2018. 3D printing of porous scaffolds with controlled porosity and pore size values. Materials 11, 1532. https://doi.org/10.3390/ma11091532.
Castro, A.P.G., Pires, T., Santos, J.E., Gouveia, B.P., Fernandes, P.R., 2019. Permeability versus design in TPMS scaffolds. Materials 12, 1313. https://doi.org/10.3390/ma12081313.
Chen, G., Chen, N., Wang, Q., 2019. Fabrication and properties of poly(vinyl alcohol)/β-tricalcium phosphate composite scaffolds via fused deposition modeling for bone tissue engineering. Compos. Sci. Technol. 172, 17–28. https://doi.org/10.1016/j.compscitech.2019.01.004.
Chen, Z., Yan, X., Yin, S., Liu, L., Liu, X., Zhao, G., Ma, W., Qi, W., Ren, Z., Liao, H., Liu, M., Cai, D., Fang, H., 2020. Influence of the pore size and porosity of selective laser melted Ti6Al4V ELI porous scaffold on cell proliferation, osteogenesis and bone ingrowth. Mater. Sci. Eng. C 106, 110289. https://doi.org/10.1016/j.msec.2019.110289.
Cohen, D.J., Cheng, A., Sahingur, K., Clohessy, R.M., Hopkins, L.B., Boyan, B.D., Schwartz, Z., 2017. Performance of laser sintered Ti–6Al–4V implants with bone-inspired porosity and micro/nanoscale surface roughness in the rabbit femur. Biomed. Mater. 12, 025021 https://doi.org/10.1088/1748-605X/aa6810.
Diao, J., OuYang, J., Deng, T., Liu, X., Feng, Y., Zhao, N., Mao, C., Wang, Y., 2018. 3D-Plotted beta-tricalcium phosphate scaffolds with smaller pore sizes improve in vivo bone regeneration and biomechanical properties in a critical-sized calvarial defect rat model. Adv. Healthc. Mater. 7, 1800441 https://doi.org/10.1002/adhm.201800441.
Dias, M.R., Fernandes, P.R., Guedes, J.M., Hollister, S.J., 2012. Permeability analysis of scaffolds for bone tissue engineering. J. Biomech. 45, 938–944. https://doi.org/10.1016/j.jbiomech.2012.01.019.
Diego, R.B., Estellés, J.M., Sanz, J.A., García-Aznar, J.M., Sánchez, M.S., 2007. Polymer scaffolds with interconnected spherical pores and controlled architecture for tissue engineering: fabrication, mechanical properties, and finite element modeling. J. Biomed. Mater. Res. B Appl. Biomater. 81B, 448–455. https://doi.org/10.1002/jbm.b.30683.
Entezari, A., Fang, J., Sue, A., Zhang, Z., Swain, M.V., Li, Q., 2016. Yielding behaviors of polymeric scaffolds with implications to tissue engineering. Mater. Lett. 184, 108–111. https://doi.org/10.1016/j.matlet.2016.07.149.

Findik, F., 2017. Titanium based biomaterials. Curr. Trends Biomed. Eng. Biosci. 7, 52–54.
Fyhrie, D.P., Kimura, J.H., 1999. Cancellous bone biomechanics. J. Biomech. 32, 1139–1148. https://doi.org/10.1016/S0021-9290(99)00114-1.
Garzon-Hernandez, S., Garcia-Gonzalez, D., Jérusalem, A., Arias, A., 2020. Design of FDM 3D printed polymers: an experimental-modelling methodology for the prediction of mechanical properties. Mater. Des. 188, 108414 https://doi.org/10.1016/j.matdes.2019.108414.
Ghouse, S., Reznikov, N., Boughton, O.R., Babu, S., Ng, K.C.G., Blunn, G., Cobb, J.P., Stevens, M.M., Jeffers, J.R.T., 2019. The design and in vivo testing of a locally stiffness-matched porous scaffold. Appl. Mater. Today 15, 377–388. https://doi.org/10.1016/j.apmt.2019.02.017.
Gomez-Gras, G., Jerez-Mesa, R., Travieso-Rodriguez, J.A., Lluma-Fuentes, J., 2018. Fatigue performance of fused filament fabrication PLA specimens. Mater. Des. 140, 278–285. https://doi.org/10.1016/j.matdes.2017.11.072.
Gregor, A., Filová, E., Novák, M., Kronek, J., Chlup, H., Buzgo, M., Blahnová, V., Lukášová, V., Bartoš, M., Nečas, A., Hošek, J., 2017. Designing of PLA scaffolds for bone tissue replacement fabricated by ordinary commercial 3D printer. J. Biol. Eng. 11, 31. https://doi.org/10.1186/s13036-017-0074-3.
Grémare, A., Guduric, V., Bareille, R., Heroguez, V., Latour, S., L'heureux, N., Fricain, J.-C., Catros, S., Nihouannen, D.L., 2018. Characterization of printed PLA scaffolds for bone tissue engineering. J. Biomed. Mater. Res. 106, 887–894. https://doi.org/10.1002/jbm.a.36289.
Gualandi, C., White, L.J., Chen, L., Gross, R.A., Shakesheff, K.M., Howdle, S.M., Scandola, M., 2010. Scaffold for tissue engineering fabricated by non-isothermal supercritical carbon dioxide foaming of a highly crystalline polyester. Acta Biomater. 6, 130–136. https://doi.org/10.1016/j.actbio.2009.07.020.
Han, C., Yan, C., Wen, S., Xu, T., Li, S., Liu, J., Wei, Q., Shi, Y., 2017. Effects of the unit cell topology on the compression properties of porous Co-Cr scaffolds fabricated via selective laser melting. Rapid Prototyp. J. 23, 16–27. https://doi.org/10.1108/RPJ-08-2015-0114.
Hanon, M.M., Kovács, M., Zsidai, L., 2019. Tribology behaviour investigation of 3D printed polymers. Int. Rev. Appl. Sci. Eng. 10, 173–181. https://doi.org/10.1556/1848.2019.0021.
Hedayati, R., Sadighi, M., Mohammadi-Aghdam, M., Zadpoor, A.A., 2016. Mechanical properties of regular porous biomaterials made from truncated cube repeating unit cells: analytical solutions and computational models. Mater. Sci. Eng. C 60, 163–183. https://doi.org/10.1016/j.msec.2015.11.001.
Hedayati, S.K., Behravesh, A.H., Hasannia, S., Bagheri Saed, A., Akhoundi, B., 2020. 3D printed PCL scaffold reinforced with continuous biodegradable fiber yarn: a study on mechanical and cell viability properties. Polym. Test. 83, 106347 https://doi.org/10.1016/j.polymertesting.2020.106347.
Hu, J., Wang, J.H., Wang, R., Yu, X.B., Liu, Y., Baur, D.A., 2019. Analysis of biomechanical behavior of 3D printed mandibular graft with porous scaffold structure designed by topological optimization. 3D Print Med 5, 5. https://doi.org/10.1186/s41205-019-0042-2.
Jing, X., Li, H., Mi, H.-Y., Liu, Y.-J., Tan, Y.-M., 2019. Fabrication of three-dimensional fluffy nanofibrous scaffolds for tissue engineering via electrospinning and CO2 escaping foaming. Ind. Eng. Chem. Res. 58, 9412–9421. https://doi.org/10.1021/acs.iecr.9b00935.
Kacmarcik, J., Spahic, D., Varda, K., Porca, E., Zaimovic-Uzunovic, N., 2018. An investigation of geometrical accuracy of desktop 3D printers using CMM. IOP Conf. Ser. Mater. Sci. Eng. 393, 012085 https://doi.org/10.1088/1757-899X/393/1/012085.
Kadkhodapour, J., Montazerian, H., Darabi, A.Ch, Anaraki, A.P., Ahmadi, S.M., Zadpoor, A.A., Schmauder, S., 2015. Failure mechanisms of additively manufactured porous biomaterials: effects of porosity and type of unit cell. J. Mech. Behav. Biomed. Mater. 50, 180–191. https://doi.org/10.1016/j.jmbbm.2015.06.012.
Kelly, C.N., Francovich, J., Julmi, S., Safranski, D., Guldberg, R.E., Maier, H.J., Gall, K., 2019. Fatigue behavior of As-built selective laser melted titanium scaffolds with sheet-based gyroid microarchitecture for bone tissue engineering. Acta Biomater. 94, 610–626. https://doi.org/10.1016/j.actbio.2019.05.046.
Knychala, J., Bouropoulos, N., Catt, C.J., Katsamenis, O.L., Please, C.P., Sengers, B.G., 2013. Pore geometry regulates early stage human bone marrow cell tissue formation and organisation. Ann. Biomed. Eng. 41, 917–930. https://doi.org/10.1007/s10439-013-0748-z.
Lee, D.J., Kwon, J., Kim, Y.-I., Wang, X., Wu, T.-J., Lee, Y.-T., Kim, S., Miguez, P., Ko, C.-C., 2019. Effect of pore size in bone regeneration using polydopamine-laced hydroxyapatite collagen calcium silicate scaffolds fabricated by 3D mould printing technology. Orthod. Craniofac. Res. 22, 127–133. https://doi.org/10.1111/ocr.12261.
Lerebours, C., Thomas, C.D.L., Clement, J.G., Buenzli, P.R., Pivonka, P., 2015. The relationship between porosity and specific surface in human cortical bone is subject specific. Bone 72, 109–117. https://doi.org/10.1016/j.bone.2014.11.016.
Li, X., Saeed, S.-S., Beni, M.H., Morovvati, M.R., Angili, S.N., Toghraie, D., Khandan, A., Khan, A., 2021. Experimental measurement and simulation of mechanical strength and biological behavior of porous bony scaffold coated with alginate-hydroxyapatite for femoral applications. Compos. Sci. Technol. 214, 108973 https://doi.org/10.1016/j.compscitech.2021.108973.
Liao, S.S., Cui, F.Z., Zhang, W., Feng, Q.L., 2004. Hierarchically biomimetic bone scaffold materials: nano-HA/collagen/PLA composite. J. Biomed. Mater. Res. B Appl. Biomater. 69B, 158–165. https://doi.org/10.1002/jbm.b.20035.
Liedert, A., Kaspar, D., Augat, P., Ignatius, A., Claes, L., 2005. Mechanobiology of bone tissue and bone cells. In: Kamkin, A., Kiseleva, I. (Eds.), Mechanosensitivity in Cells and Tissues. Academia, Moscow.
Limmahakhun, S., Oloyede, A., Sitthiseripratip, K., Xiao, Y., Yan, C., 2017. Stiffness and strength tailoring of cobalt chromium graded cellular structures for stress-shielding reduction. Mater. Des. 114, 633–641. https://doi.org/10.1016/j.matdes.2016.11.090.
Lin, C.Y., Kikuchi, N., Hollister, S.J., 2004. A novel method for biomaterial scaffold internal architecture design to match bone elastic properties with desired porosity. J. Biomech. 37, 623–636. https://doi.org/10.1016/j.jbiomech.2003.09.029.
Liu, F., Zhang, D.Z., Zhang, P., Zhao, M., Jafar, S., 2018. Mechanical properties of optimized diamond lattice structure for bone scaffolds fabricated via selective laser melting. Materials 11, 374. https://doi.org/10.3390/ma11030374.
Liverani, E., Rogati, G., Pagani, S., Brogini, S., Fortunato, A., Caravaggi, P., 2021. Mechanical interaction between additive-manufactured metal lattice structures and bone in compression: implications for stress shielding of orthopaedic implants. J. Mech. Behav. Biomed. Mater. 121, 104608. https://doi.org/10.1016/j.jmbbm.2021.104608.
Lu, Y., Cheng, L., Yang, Z., Li, J., Zhu, H., 2020. Relationship between the morphological, mechanical and permeability properties of porous bone scaffolds and the underlying microstructure. PLoS One 15, e0238471. https://doi.org/10.1371/journal.pone.0238471.
Martin, R., 1984. Porosity and specific surface of bone. Crit. Rev. Biomed. Eng. 10, 179–222.
D20 Committee, n.d. Test Method for Compressive Properties of Rigid Plastics. ASTM International. https://doi.org/10.1520/D0695-15 .
MATLAB R2021a, n.d..
MATLAB, 2012. The MathWorks, Inc., Natick, Massachusetts, United States.
Mazzanti, V., Malagutti, L., Mollica, F., 2019. FDM 3D printing of polymers containing natural fillers: a review of their mechanical properties. Polymers 11, 1094. https://doi.org/10.3390/polym11071094.
Montazerian, H., Zhianmanesh, M., Davoodi, E., Milani, A.S., Hoorfar, M., 2017. Longitudinal and radial permeability analysis of additively manufactured porous scaffolds: effect of pore shape and porosity. Mater. Des. 122, 146–156. https://doi.org/10.1016/j.matdes.2017.03.006.
Murphy, C.M., Haugh, M.G., O'Brien, F.J., 2010. The effect of mean pore size on cell attachment, proliferation and migration in collagen–glycosaminoglycan scaffolds for bone tissue engineering. Biomaterials 31, 461–466. https://doi.org/10.1016/j.biomaterials.2009.09.063.
Naderi, A., Zhang, B., Belgodere, J.A., Sunder, K., Palardy, G., 2021. Improved biocompatible, flexible mesh composites for implant applications via hydroxyapatite coating with potential for 3-dimensional extracellular matrix network and bone regeneration. ACS Appl. Mater. Interfaces 13, 26824–26840. https://doi.org/10.1021/acsami.1c09034.
Navarro, M., Michiardi, A., Castaño, O., Planell, J. a, 2008. Biomaterials in orthopaedics. J. R. Soc. Interface 5, 1137–1158. https://doi.org/10.1098/rsif.2008.0151.
Niaza, K.V., Senatov, F.S., Stepashkin, A., Anisimova, N.Y., Kiselevsky, M.V., 2017. Long-term creep and impact strength of biocompatible 3D-printed PLA-based scaffolds. Nano Hybrids Compos. 13, 15–20. https://doi.org/10.4028/www.scientific.net/NHC.13.15.
Novotna, L., Kucera, L., Hampl, A., Drdlik, D., Cihlar, J., Cihlar, J., 2019. Biphasic calcium phosphate scaffolds with controlled pore size distribution prepared by in-situ foaming. Mater. Sci. Eng. C 95, 363–370. https://doi.org/10.1016/j.msec.2018.03.022.
Onal, E., Frith, J.E., Jurg, M., Wu, X., Molotnikov, A., 2018. Mechanical properties and in vitro behavior of additively manufactured and functionally graded Ti6Al4V porous scaffolds. Metals 8, 200. https://doi.org/10.3390/met8040200.
Ostrowska, B., Luca, A.D., Moroni, L., Swieszkowski, W., 2016. Influence of internal pore architecture on biological and mechanical properties of three-dimensional fiber deposited scaffolds for bone regeneration. J. Biomed. Mater. Res. 104, 991–1001. https://doi.org/10.1002/jbm.a.35637.
Ouyang, P., Dong, H., He, X., Cai, X., Wang, Y., Li, J., Li, H., Jin, Z., 2019. Hydromechanical mechanism behind the effect of pore size of porous titanium scaffolds on osteoblast response and bone ingrowth. Mater. Des. 183, 108151 https://doi.org/10.1016/j.matdes.2019.108151.
Pierantozzi, D., Scalzone, A., Jindal, S., Stīpniece, L., Šalma-Ancāne, K., Dalgarno, K., Gentile, P., Mancuso, E., 2020. 3D printed Sr-containing composite scaffolds: effect of structural design and material formulation towards new strategies for bone tissue engineering. Compos. Sci. Technol. 191, 108069 https://doi.org/10.1016/j.compscitech.2020.108069.
Pires, T., Santos, J., Ruben, R.B., Gouveia, B.P., Castro, A.P.G., Fernandes, P.R., 2021. Numerical-experimental analysis of the permeability-porosity relationship in triply periodic minimal surfaces scaffolds. J. Biomech. 117, 110263. https://doi.org/10.1016/j.jbiomech.2021.110263.
Poh, P.S.P., Valainis, D., Bhattacharya, K., van Griensven, M., Dondl, P., 2019. Optimization of bone scaffold porosity distributions. Sci. Rep. 9, 9170. https://doi.org/10.1038/s41598-019-44872-2.
Qiu, Z.-Y., Cui, Y., Wang, X.-M., 2019. Chapter 1 - natural bone tissue and its biomimetic. In: Wang, X.-M., Qiu, Z.-Y., Cui, H. (Eds.), Mineralized Collagen Bone Graft Substitutes, Woodhead Publishing Series in Biomaterials. Woodhead Publishing, pp. 1–22. https://doi.org/10.1016/B978-0-08-102717-2.00001-1.
Rodrigues, N., Benning, M., Ferreira, A.M., Dixon, L., Dalgarno, K., 2016. Manufacture and characterisation of porous PLA scaffolds. Procedia CIRP, The Second CIRP Conference on Biomanufacturing 49, 33–38. https://doi.org/10.1016/j.procir.2015.07.025.
Ronca, D., Langella, F., Chierchia, M., D'Amora, U., Russo, T., Domingos, M., Gloria, A., Bartolo, P., Ambrosio, L., 2016. Bone tissue engineering: 3D PCL-based nanocomposite scaffolds with tailored properties. In: Procedia CIRP, the Second

CIRP Conference on Biomanufacturing, vol. 49, pp. 51–54. https://doi.org/10.1016/j.procir.2015.07.028.

Roosa, S.M.M., Kemppainen, J.M., Moffitt, E.N., Krebsbach, P.H., Hollister, S.J., 2010. The pore size of polycaprolactone scaffolds has limited influence on bone regeneration in an in vivo model. J. Biomed. Mater. Res. 92A, 359–368. https://doi.org/10.1002/jbm.a.32381.

Rumpler, M., Woesz, A., Dunlop, J.W.C., van Dongen, J.T., Fratzl, P., 2008. The effect of geometry on three-dimensional tissue growth. J. R. Soc. Interface 5, 1173–1180. https://doi.org/10.1098/rsif.2008.0064.

Sahmani, S., Khandan, A., Esmaeili, S., Saber-Samandari, S., Ghadiri Nejad, M., Aghdam, M.M., 2020. Calcium phosphate-PLA scaffolds fabricated by fused deposition modeling technique for bone tissue applications: fabrication, characterization and simulation. Ceram. Int. 46, 2447–2456. https://doi.org/10.1016/j.ceramint.2019.09.238.

Santos, J., Pires, T., Gouveia, B.P., Castro, A.P.G., Fernandes, P.R., 2020. On the permeability of TPMS scaffolds. J. Mech. Behav. Biomed. Mater. 110, 103932. https://doi.org/10.1016/j.jmbbm.2020.103932.

Sanz-Herrera, J.A., Garcia-Aznar, J.M., Doblare, M., 2008. A mathematical model for bone tissue regeneration inside a specific type of scaffold. Biomech. Model. Mechanobiol. 7, 355–366. https://doi.org/10.1007/s10237-007-0089-7.

Senatov, F.S., Niaza, K.V., Zadorozhnyy, M.Yu, Maksimkin, A.V., Kaloshkin, S.D., Estrin, Y.Z., 2016. Mechanical properties and shape memory effect of 3D-printed PLA-based porous scaffolds. J. Mech. Behav. Biomed. Mater. 57, 139–148. https://doi.org/10.1016/j.jmbbm.2015.11.036.

Skalka, P., Slámečka, K., Montufar, E.B., Čelko, L., 2019. Estimation of the effective elastic constants of bone scaffolds fabricated by direct ink writing. J. Eur. Ceram. Soc. 39, 1586–1594. https://doi.org/10.1016/j.jeurceramsoc.2018.12.024.

Soro, N., Attar, H., Brodie, E., Veidt, M., Molotnikov, A., Dargusch, M.S., 2019. Evaluation of the mechanical compatibility of additively manufactured porous Ti–25Ta alloy for load-bearing implant applications. J. Mech. Behav. Biomed. Mater. 97, 149–158. https://doi.org/10.1016/j.jmbbm.2019.05.019.

Sudarmadji, N., Tan, J.Y., Leong, K.F., Chua, C.K., Loh, Y.T., 2011. Investigation of the mechanical properties and porosity relationships in selective laser-sintered polyhedral for functionally graded scaffolds. Acta Biomater. 7, 530–537. https://doi.org/10.1016/j.actbio.2010.09.024.

Torres-Sanchez, C., Al Mushref, F.R.A., Norrito, M., Yendall, K., Liu, Y., Conway, P.P., 2017. The effect of pore size and porosity on mechanical properties and biological response of porous titanium scaffolds. Mater. Sci. Eng. C 77, 219–228. https://doi.org/10.1016/j.msec.2017.03.249.

Van Bael, S., Chai, Y.C., Truscello, S., Moesen, M., Kerckhofs, G., Van Oosterwyck, H., Kruth, J.-P., Schrooten, J., 2012. The effect of pore geometry on the in vitro biological behavior of human periosteum-derived cells seeded on selective laser-melted Ti6Al4V bone scaffolds. Acta Biomater. 8, 2824–2834. https://doi.org/10.1016/j.actbio.2012.04.001.

Wang, W., Zhang, B., Li, M., Li, J., Zhang, C., Han, Y., Wang, L., Wang, K., Zhou, C., Liu, L., Fan, Y., Zhang, X., 2021. 3D printing of PLA/n-HA composite scaffolds with customized mechanical properties and biological functions for bone tissue engineering. Compos. B Eng. 224, 109192 https://doi.org/10.1016/j.compositesb.2021.109192.

Wieding, J., Wolf, A., Bader, R., 2014. Numerical optimization of open-porous bone scaffold structures to match the elastic properties of human cortical bone. J. Mech. Behav. Biomed. Mater. 37, 56–68. https://doi.org/10.1016/j.jmbbm.2014.05.002.

Yang, L., Han, C., Wu, H., Hao, L., Wei, Q., Yan, C., Shi, Y., 2020. Insights into unit cell size effect on mechanical responses and energy absorption capability of titanium graded porous structures manufactured by laser powder bed fusion. J. Mech. Behav. Biomed. Mater. 109, 103843. https://doi.org/10.1016/j.jmbbm.2020.103843.

Yin, S., Zhang, W., Zhang, Z., Jiang, X., 2019. Recent advances in scaffold design and material for vascularized tissue-engineered bone regeneration. Adv. Healthc. Mater. 8, 1801433 https://doi.org/10.1002/adhm.201801433.

A. Zadpoor, A., 2015. Bone tissue regeneration: the role of scaffold geometry Biomater. Sci. 3, 231–245. https://doi.org/10.1039/C4BM00291A.

Zaharin, H.A., Abdul Rani, A.M., Azam, F.I., Ginta, T.L., Sallih, N., Ahmad, A., Yunus, N. A., Zulkifli, T.Z.A., 2018. Effect of unit cell type and pore size on porosity and mechanical behavior of additively manufactured Ti6Al4V scaffolds. Materials 11, 2402. https://doi.org/10.3390/ma11122402.

Zhang, J., Wehrle, E., Adamek, P., Paul, G.R., Qin, X.-H., Rubert, M., Müller, R., 2020. Optimization of mechanical stiffness and cell density of 3D bioprinted cell-laden scaffolds improves extracellular matrix mineralization and cellular organization for bone tissue engineering. Acta Biomater. 114, 307–322. https://doi.org/10.1016/j.actbio.2020.07.016.

Zhang, B., Wang, L., Song, P., Pei, X., Sun, H., Wu, L., Zhou, C., Wang, K., Fan, Y., Zhang, X., 2021. 3D printed bone tissue regenerative PLA/HA scaffolds with comprehensive performance optimizations. Mater. Des. 201, 109490 https://doi.org/10.1016/j.matdes.2021.109490.

Zhao, S., Arnold, M., Ma, S., Abel, R.L., Cobb, J.P., Hansen, U., Boughton, O., 2018. Standardizing compression testing for measuring the stiffness of human bone. Bone Joint Res. 7, 524–538. https://doi.org/10.1302/2046-3758.78.BJR-2018-0025.R1.